fractal and fractional

Article

Diabase Intrusion-Induced Changes in Shale Pore Structure in Subei Basin: Insights from Mono- and Multifractal Analysis of N_2 Adsorption

Zuxian Hua [1,2], Xiaoping Liu [1,2,*], Biao Sun [1,2], Tian Liu [1,2], Qidong Liu [3], Hongliang Duan [3], Shili Liu [3], Yue Zheng [1,2], Wendi Peng [1,2] and Wenhui Xie [1,2]

[1] National Key Laboratory of Petroleum Resources and Engineering, China University of Petroleum (Beijing), Beijing 102249, China; hzx.c@outlook.com (Z.H.); biao199508@foxmail.com (B.S.); 13804341768@163.com (T.L.); yue385077@gmail.com (Y.Z.); 18180521923@163.com (W.P.); xwh551214@163.com (W.X.)
[2] College of Geosciences, China University of Petroleum (Beijing), Beijing 102249, China
[3] Research Institute of Exploration and Development, SINOPEC Jiangsu Oilfield Company, Yangzhou 225009, China; liuqd.jsyt@sinopec.com (Q.L.); duanhl.jsyt@sinopec.com (H.D.); liusl.jsyt@sinopec.com (S.L.)
* Correspondence: liuxiaoping@cup.edu.cn

Abstract: Diabase intrusion is a common geological phenomenon in lacustrine shale formations in continental basins in China, which has important effects on the physical and chemical properties of shale oil reservoirs. In this paper, we systematically analyzed the pore structure of diabase-intruded lacustrine shale in the Gaoyou sag of the Subei Basin using geochemical tests, thin-section observation, argon ion polishing scanning electron microscopy (SEM), low-temperature nitrogen adsorption experiments (LTNA), and other methods combined with monofractal and multifractal theories. The results show that the intrusion metamorphic segments are a diabase zone, hornfels zone, slate zone, and normal shale zone from the intrusion center. The pores of hornfels and slate are mostly oriented and dissolution is obvious. Many microfractures and secondary minerals such as quartz and chlorite are observed. The pore volumes of diabase and hornfels are small, while those of slate and normal shale are larger. The monofractal dimensions D_1 and D_2 of the intrusion segment show a general trend of decreasing first and then increasing from the intrusion center to the shale zone. The multifractal parameters' H index decreases gradually from the lower normal shale to the upper metamorphic zone hornfels, while $\Delta\alpha$ and Rd increase gradually. The total organic carbon (TOC) content of the intrusion zone has little effect on the pore structure, and the fractal characteristics fluctuate weakly, while the vitrinite reflectivity (R_o) value change has a significant impact on the monofractal characteristics of the shale pore. Pore volume also affects the pore heterogeneity; the larger the specific surface area (SSA) and total pore volume (TPV), the lower the pore heterogeneity and the higher the surface roughness and pore connectivity. The diabase intrusion caused three modification mechanisms of mechanical squeezing, the thermal effect, and chemical action on the shale surrounding rocks, resulting in different degrees of pore formation or change. The pore evolution model of the metamorphic belt with the combined action of "mechanical-thermal-chemical" is established, and the influence of diabase intrusion on the pore types and pore size distribution (PSD) of shale reservoirs is quantitatively described, providing a new perspective and method for understanding the impact of diabase intrusion on the characteristics and exploration potential of shale oil reservoirs.

Keywords: diabase intrusion; metamorphic shale; pore structure; fractal; Funing Formation; Subei Basin

check for updates

Citation: Hua, Z.; Liu, X.; Sun, B.; Liu, T.; Liu, Q.; Duan, H.; Liu, S.; Zheng, Y.; Peng, W.; Xie, W. Diabase Intrusion-Induced Changes in Shale Pore Structure in Subei Basin: Insights from Mono- and Multifractal Analysis of N_2 Adsorption. *Fractal Fract.* **2024**, *8*, 737. https://doi.org/10.3390/fractalfract8120737

Academic Editor: Alex Elías-Zúñiga

Received: 22 October 2024
Revised: 24 November 2024
Accepted: 29 November 2024
Published: 14 December 2024

Copyright: © 2024 by the authors. Licensee MDPI, Basel, Switzerland. This article is an open access article distributed under the terms and conditions of the Creative Commons Attribution (CC BY) license (https://creativecommons.org/licenses/by/4.0/).

1. Introduction

Shale and volcanic oil reservoirs are both key areas of petroleum exploration and development, and oil reservoirs related to magmatic activity have always concerned many scholars [1]. The existing exploration targets are mostly volcanic clastic rock reservoirs and conventional reservoirs near volcanic rocks [2–5], while intrusive rocks and shale surrounding rocks receive relatively less attention [6], and the influence of the relationship between intrusive rocks and shale surrounding rocks, especially the influence on the micropore structure, is lacking in-depth research.

The high-temperature diabase intrusion from deep strata can have profound effects on the adjacent mudstone, leading to a series of geological processes that alter the original pore characteristics of the shale and create a unique hydrocarbon accumulation mode. Specifically, the thermal energy released by the diabase intrusion causes significant thermal alteration of the mudstone. This thermal alteration can lead to the maturation of organic matter, enhancing the generation and expulsion of hydrocarbons [7]. Additionally, the elevated temperatures can induce mineral transformations, such as the conversion of smectite to illite, which can affect the porosity and permeability of the shale [8].

The mechanical impact of the diabase intrusion is equally significant. The intrusion can cause extrusion fractures in the surrounding mudstone, creating new pathways for fluid migration. These fractures can significantly increase the permeability of the shale, facilitating the movement of hydrocarbons [9].

The mechanism and extent of the influence of diabase intrusion on the shale pore structure are still unclear, and there are some controversies. Some studies believe that diabase intrusion can improve the pore structure of shale oil reservoirs by generating secondary pores and microfractures [10–12], while other studies believe that diabase intrusion can cause pore blockage by increasing thermal maturity and compaction, thereby deteriorating the porosity of shale oil reservoirs [13] and the process and degree of transformation need to be refined.

Diabase is a typical shallow intrusive rock which is widely distributed in the world. A large number of diabase intrusions were found in the Subei Basin, Songliao Basin, Bohai Bay Basin, and Santanghu Basin in China. Among them, the diabase intrusion area in the Subei Basin can reach up to 1000 km^2, and good shale oil and gas have been observed in the shale strata of the Gaoyou Sag, Baiju Sag, and Hai'an Sag [14,15]. This study starts by describing the petrology, geochemistry, and pore characteristics of shale reservoirs and uses the monofractal and multifractal theory [16] to analyze how diabase transforms the micropore structure of shale surrounding rocks. Then, a transformation model of diabase for shale surrounding rocks is proposed. This study quantitatively analyzes the micropore characteristics of intrusive rocks and metamorphic shale surrounding rocks and compares pore structures and fractal parameter characteristics of shale with different metamorphic degrees, providing a useful case for this type of unconventional oil and gas reservoir exploration, which can be better applied to intrusive rock strata such as the Gunnedah Basin in Australia [17] and the Sverdrup Basin in the Arctic region of Canada [18], expanding the research field of shale and volcanic oil reservoirs.

2. Geological Setting

The Subei Basin, a large Mesozoic–Cenozoic sedimentary basin in Jiangsu Province, China, spans about 3.6×10^4 km^2 (Figure 1a,b). It has undergone multiple tectonic cycles and has a complex geological history. The Gaoyou Sag, a sub-basin within the Subei Basin, covers about 2600 km^2 and has a spoon-shaped structure with a high northwest and a low southeast, bounded by a southern fault step zone. According to the tectonic position, it can be divided into three parts, the northern slope, deep depression zone, and the fault step zone (Figure 1c) [19]. The Funing Formation (Fm.) is one of the main shale oil layers in the basin, influenced by the Paleogene lacustrine transgression during the sedimentary period [20]. It consists of four sub-sections, of which the second member of the Funing Fm. is dominated by dark mud shale, a fine-grained sedimentary rock of a deep–semi-deep lake environment. It is a petroliferous shale oil reservoir section (Figure 1d). This study focuses on the diabase and metamorphic shale rock of the Funing Fm. in the north-central part of the Gaoyou Sag. The intrusion range can reach 1000 km^2 and the single-layer thickness range is about 10–200 m [5,21,22].

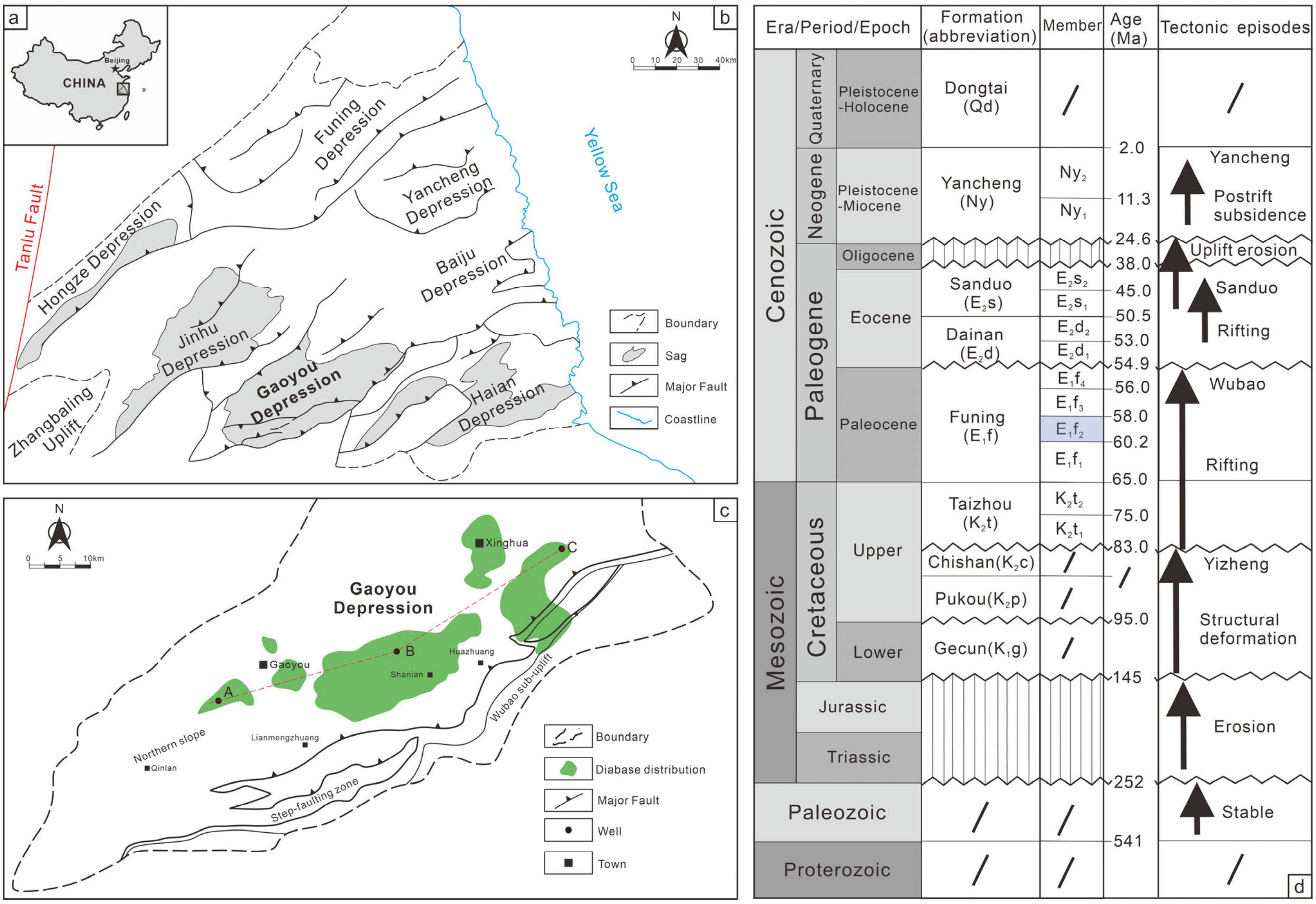

Figure 1. (**a**) Location of the research area; (**b**) division of the basic tectonic units of the north Subei Basin location; (**c**) Gaoyou Sag substructural units and diabase distribution area; (**d**) stratigraphic characteristics of the north Subei Basin.

3. Materials and Methods

This research collected 11 core samples from wells A, B, and C in the Gaoyou Sag of the Subei Basin (Figure 2), and the well locations are shown in Figure 1c. This study employed SEM, LTNA, geochemical analysis, and mono- and multifractal analysis to characterize the structure and properties of various materials (Table 1).

N_2 adsorption is widely used for determining the specific surface area and pore size distribution of porous materials due to its non-destructive nature and high sensitivity to micropores and mesopores. However, it has certain limitations, especially when characterizing macropores or highly hydrophobic materials. In contrast, MIP is more suitable for measuring larger pores and can provide detailed information on the pore throat size distribution, which is crucial for understanding the transport properties of porous media. Mercury intrusion porosimetry (MIP), however, may not be as effective in detecting microporosity and can sometimes cause structural damage to fragile samples. Since this study takes hornfels, slate, and shale as the research objects and mainly focuses on micropores and mesopores, N_2 adsorption will be more suitable.

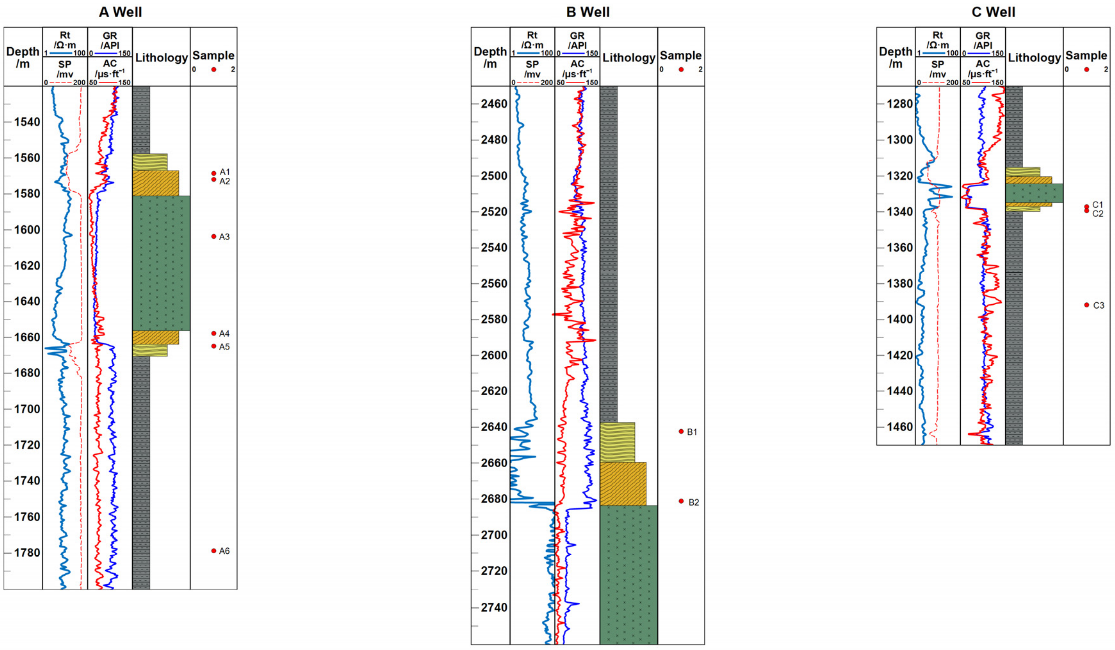

Figure 2. Electrical characteristics and sampling locations of intrusion sections of wells A, B, and C in Gaoyou Sag. (Tips: well location distribution is shown in Figure 1c.)

Table 1. Sampling information, pore structure, and geochemical parameters of the intrusive metamorphic section samples.

Sample ID	Well No.	Depth /m	Lithology	Surface Area /m^2·g^{-1}	Pore Volume /cc.g^{-1}	TOC /%	R$_o$ /%	S$_1$ /mg.g^{-1}	S$_2$ /mg.g^{-1}	T$_{max}$ /°C
A1	A	1568.47	Hornfels	5.078	0.014	0.98	2.20	0.29	0.17	402
A2	A	1571.87	Hornfels	5.106	0.013	1.30	2.17	0.44	0.27	409
A3	A	1603.64	Diabase	2.958	0.008	0.07	/	0.01	0.01	435
A4	A	1657.65	Hornfels	7.691	0.02	2.04	1.35	0.61	0.23	408
A5	A	1664.82	Slate	16.4	0.03	0.08	1.27	0.01	0.01	498
A6	A	1778.73	Shale	14.95	0.023	0.79	0.52	0.11	1.96	445
B1	B	2642.31	Slate	2.903	0.009	0.10	/	0.02	0.03	381
B2	B	2681.12	Hornfels	6.707	0.018	0.05	/	0.03	0.04	368
C1	C	1337.14	Hornfels	7.04	0.014	0.07	/	0.28	0.83	436
C2	C	1339.78	Slate	19.676	0.052	0.89	/	0.13	0.86	409
C3	C	1391.80	Shale	33.688	0.063	/	/	0.07	1.56	427

The experimental procedure consisted of the following steps: several materials were selected and ground into fine powders. Scanning electron microscopy (SEM) was performed on each powder sample using an electron microscope to examine their morphology. The SEM images of each sample were obtained and analyzed. Nitrogen adsorption was then carried out on each sample using an adsorption analyzer. The LTNA isotherms of each sample were recorded and their SSA and PSD were calculated by supporting software. Furthermore, the monofractal and multifractal theory were applied to each sample to perform multifractal analysis, which yielded their multifractal spectrum and singularity spectrum. These spectra were compared among different samples to evaluate their scaling behavior and complexity.

3.1. Scanning Electron Microscopy

The mudstone, slate, and gneiss samples were cut into standardized cubic shapes and polished meticulously. The initial sanding with coarse-grit sandpaper created a flat surface, followed by finer-grit sanding to refine the texture. An argon ion beam was finally employed to achieve a highly polished surface, then the samples were sprayed with carbon to avoid contamination and oxidation. The prepared samples were observed using the advanced Carl Zeiss electron microscope at the National Key Laboratory of China University of Petroleum, Beijing, which enabled a deep analysis of their mineralogical and structural characteristics. This rigorous sample preparation process, coupled with advanced equipment, facilitated the production of high-quality and accurate images for a thorough understanding of the studied rock samples.

3.2. N_2 Adsorption Experiment

Nitrogen gas adsorption is a powerful technique for measuring the SSA and PSD of porous materials. Here, this research performed N_2 gas adsorption and desorption experiments on 11 carefully selected samples that were crushed to a particle size of 40–60 mesh, using the Micromeritics ASAP 2460 instrument from Micromeritics Instrument Corporation U.S. Before analysis, this research dried the powder samples under vacuum and degassed them (approximately 0.5 g, <100 mesh) for 8 h at 423 K [23]. This research obtained adsorption–desorption isotherms at 77.3 K with relative pressures (P/P_0) from 0.001 to 0.995.

This research conducted N_2 gas adsorption measurements at 298 K and relative pressure (P/P_0) from 0.01 to 0.995. The data were analyzed using density functional theory (DFT) models to determine the SSA and TPV. This research also applied modified BET and DFT models to obtain various pore structure parameters, such as the SSA and PSD [24,25].

3.3. Monofractal Model and Parameters

Monofractal methods can quantify the complexity and irregularity of the material surface and structure and provide a more intuitive assessment of the micro-features of shale oil reservoir pores [26,27]. The FHH (Frenkel–Halsey–Hill) model is a widely used monofractal method that can perform monofractal analysis on the nitrogen adsorption–desorption curve with the following equation [28]:

$$\ln V = C + (D-3)\ln(\ln(P/P_0)) \tag{1}$$

where P is the equilibrium pressure, MPa; P_0 is the saturated vapor pressure, MPa; V is the adsorbed gas volume, cm^3/g; and D is the monofractal dimension.

When $D = 2$, it means that the pore surface of the sample is absolutely smooth, and when $D = 3$, it means that the pore surface is absolutely rough and complex.

3.4. Multifractal Model and Parameters

The box-counting method is used to process the LTNA data in shale porosity studies to explore the theory and calculation methods of multifractal analysis. This technique provides insights into the complex behavior of porous materials at different scales.

The box-counting method uses a set of boxes (or subintervals) of equal length to cover the total length of the research object in characterizing the multifractal behavior in porous media [29,30]. The total length is assigned to these boxes using a binary scaling method [31], $N(r)$ = 2^k (k = 0, 1, 2, 3. . .). The density probability $P_i(r)$ in box i can be expressed as [32]

$$P_i(r) = V_i(r) / \sum_{i=1}^{N(r)} V_i(r) \ \propto r^{\alpha_i} \tag{2}$$

where $V_i(r)$ is the volume of adsorbed gas in the i-th box and $N(r)$ is the total number of boxes. α_i is the singularity index, which represents the singularity degree of the research object.

For a research object with multifractal properties, $N_\alpha(r)$ follows a power law with r in the multifractal interval.

$$N_\alpha(r) \propto r^{-f(\alpha)} \tag{3}$$

where $N_\alpha(r)$ represents the number of boxes in the multifractal with $[\alpha,\ \alpha + d\alpha]$; $f(\alpha)$ corresponds to the multifractal spectrum or singularity spectrum, indicating that these boxes have the same or similar α values. $\alpha(q)$ and $f(\alpha)$ can be calculated by the following formulas [33]:

$$\alpha(q) \propto \left[\sum_{i=1}^{N(r)} \mu_i(q,r) \times logP_i(r)\right]/log(r) \tag{4}$$

$$f(q) \propto \left[\sum_{i=1}^{N(r)} \mu_i(q,r) \times log\mu_i(q,r)\right]/log(r) \tag{5}$$

where

$$\mu_i(q,r) = \frac{P_i{}^q(r)}{\sum_{i=1}^{N(r)} P_i{}^q(r)} \tag{6}$$

The denominator of $\mu(q,\ r)$ in the above equation is the partition function at scale r, also known as the statistical moment function [34], which defines $\eta(q,\ r)$ to show the magnitude of $P_i(r)$; we can obtain the power of $P_i(r)$ from q's scaling exponent as follows:

$$\eta_i(q,r) = \sum_{i=1}^{N(r)} P_i{}^q(r) \tag{7}$$

where $\tau(q)$ is the mass scaling function of the multifractal, which can be calculated by $log\eta$-$logr$, as shown below.

$$\tau_q \quad = \quad lim_{r\to 0}\frac{log\sum_{i=1}^{N(r)} P_i{}^q(r)}{log(r)} \tag{8}$$

When $\tau(q)$ is a constant for a specific q value, it shows a single regularity. When $\tau(q)$ varies with q, the research object shows multifractal characteristics. Thus, the generalized dimension D_{mq} is obtained [35].

$$D_{mq} = \frac{1}{q-1} lim_{r\to 0}\frac{log\sum_{i=1}^{N(r)} P_i{}^q(r)}{log(r)} = \frac{\tau(q)}{q-1} \tag{9}$$

When $q = 1$,

$$D_{m1} = lim_{r\to 0}\frac{log\sum_{i=1}^{N(r)} P_i(r) \times logP_i(r)}{log(r)} \tag{10}$$

The generalized dimension spectrum $D(q)$ and singularity spectrum $f(\alpha)$ are the basic descriptive parameters of multifractal behavior.

The Hurst index (H) characterizes the local autocorrelation of the PSD. It has a range of 0.5~1, and the higher the values, the better the connectivity between pores [36].

$$H = (D_{m2} + 1)/2 \tag{11}$$

The singularity width $\Delta\alpha$ quantifies the heterogeneity of the entire PSD. The larger the value, the more pore heterogeneity.

$$\Delta\alpha = \alpha_{-10} - \alpha_{10} \tag{12}$$

The Rd parameter describes the degree of deviation of the spectrum from the surrounding symmetry ($\Delta\alpha = 0$). Negative R_d values indicate a dominant pore concentration in specific regions [37,38].

$$R_d = (\alpha_0 - \alpha_{10}) - (\alpha_{-10} - \alpha_0) \tag{13}$$

Multifractal analysis based on log-transformed P/P_0 data by quantifying the gas adsorption volume density probability reveals the inherent multifractal properties of shale samples and provides valuable insights into shale porosity distribution, connectivity, and heterogeneity [39,40].

4. Results

4.1. Pore Type

The hornfels metamorphic zone in well A is a high-temperature low-pressure thermal contact metamorphic rock, with a high degree of metamorphism and being close to the intrusion center, usually at the edge or outside of the intrusion. Core samples show abundant structural microfractures, mostly filled with calcite, with irregular shapes and orientations. Some fractures intersect or cross each other, indicating that they are multi-stage fractures (Figure 3a). The fractures are filled with a white material, which is calcite sediment, indicating that these fractures underwent later hydrodynamic and chemical precipitation processes. The calcite fillings show a bright white color, contrasting with the black metamorphic mudstone. The calcite fillings have different morphologies in the fractures, with some showing a crystal structure, some showing a fibrous structure, and some showing a layered structure, indicating that the calcite sediments experienced different origins and evolution processes. Under an optical microscope, fine clay particles can be seen, tightly arranged between the particles, with a fine-grained recrystallization structure and blocky structure, being dense and hard and without obvious pores (Figure 3e). Core samples from well B show that part of the upper core is yellow-brown slate and the rest is gray-black mudstone (Figure 3b). Slate is a medium-grade metamorphic mudstone, with an obvious cleavage structure composed of fine platy or scaly metamorphic products such as mica, muscovite, illite, etc. Slate is a low-temperature low-pressure regional metamorphic rock, formed by the metamorphism of mud shale. Slate contains characteristic metamorphic minerals, such as staurolite, kyanite, sillimanite, etc. Slate has a low degree of metamorphism and has an obvious cleavage or plate structure. Slate is far from the intrusion center, usually outside or not in contact with the hornfels. The surface of the core from the diabase section in well A shows obvious large numbers of vertical fractures in the same direction. The vertical fractures are secondary fractures caused by the volume shrinkage of the diabase intrusion during cooling. They have a certain directionality and connectivity, but their number and width are not large and their contribution to oil and gas storage and migration is low (Figure 3c). The optical microscope photo shows an obvious diabasic structure, larger pyroxene particles, and smaller plagioclase particles. There are some gaps between the particles (Figure 3g).

The intrusion of diabase caused different degrees of metamorphism in the surrounding rocks, forming three different metamorphic zones, namely a hornfels zone, diabase zone, and slate zone. Each metamorphic zone has different main pore types [8]. The first line is the hornfels zone, which is the innermost layer of contact between the diabase intrusion and the surrounding rocks. Due to the dual influence of high temperature and high pressure, the shale has undergone intense metamorphism, forming hornfels. Because of the high temperature, organic matter (OM) pores are developed in the hornfels zone. The main micropore structure type of the hornfels zone comprises structural microfractures, which are secondary pores produced by the deformation and fracture of the surrounding rocks due to high temperature and pressure. The dissolution degree is severe (Figure 4a–c). The characteristics of structural microfractures are that they have a certain directionality and connectivity, but their number and width are very small and their contribution to oil and gas storage and migration is very low (Figure 4d). The second line is the diabase zone, which is the diabase intrusion itself, composed of basic minerals such as pyroxene and plagioclase, with a typical diabasic or sub-diabasic structure. The main micropore structure type of the diabase zone comprises intergranular pores, dissolution pores, and shrinkage fractures. Chlorite-filled fractures can be seen, which are secondary pores produced by the origin and evolution of the diabase intrusion itself (Figure 4e,g,h). The characteristics of intergranular pores are that they are formed by the gaps between basic minerals such as pyroxene and plagioclase, with a certain regularity and uniformity, but their size and shape are inconsistent. Dissolution pores are micropores produced by the thermal alteration of minerals under high temperature and pressure (Figure 4e,h). Shrinkage fractures are secondary fractures caused by volume shrinkage of the diabase intrusion during cooling.

The third line is the slate zone, which is the outermost layer of contact between the diabase intrusion and the surrounding rocks. It is affected by a medium degree of metamorphism, and the mud shale undergoes slatification. The characteristic of slate is that it has an obvious cleavage structure composed of fine platy or scaly metamorphic products such as mica, muscovite, illite, etc., with some gaps between cleavages (Figure 4i,h). The reservoir space in the slate zone comprises mainly secondary pores and secondary fractures, and fine OM pores can also be seen (Figure 4i,j). Primary pores are formed by gaps between cleavages and secondary fractures are formed by condensation shrinkage and dissolution (Figure 4k,l). The fourth line is the normal mudstone zone, which is mud shale that has not been affected by diabase intrusion without metamorphism. The characteristic of normal mudstone is that it has a bedding structure composed of fine clay, carbonate, siliceous particles, etc., with a small amount of pyrite. The pores in normal mudstone are mainly primary pores and secondary fractures, with some intergranular pores developed. OM pores are not developed, and the dissolution degree is small.

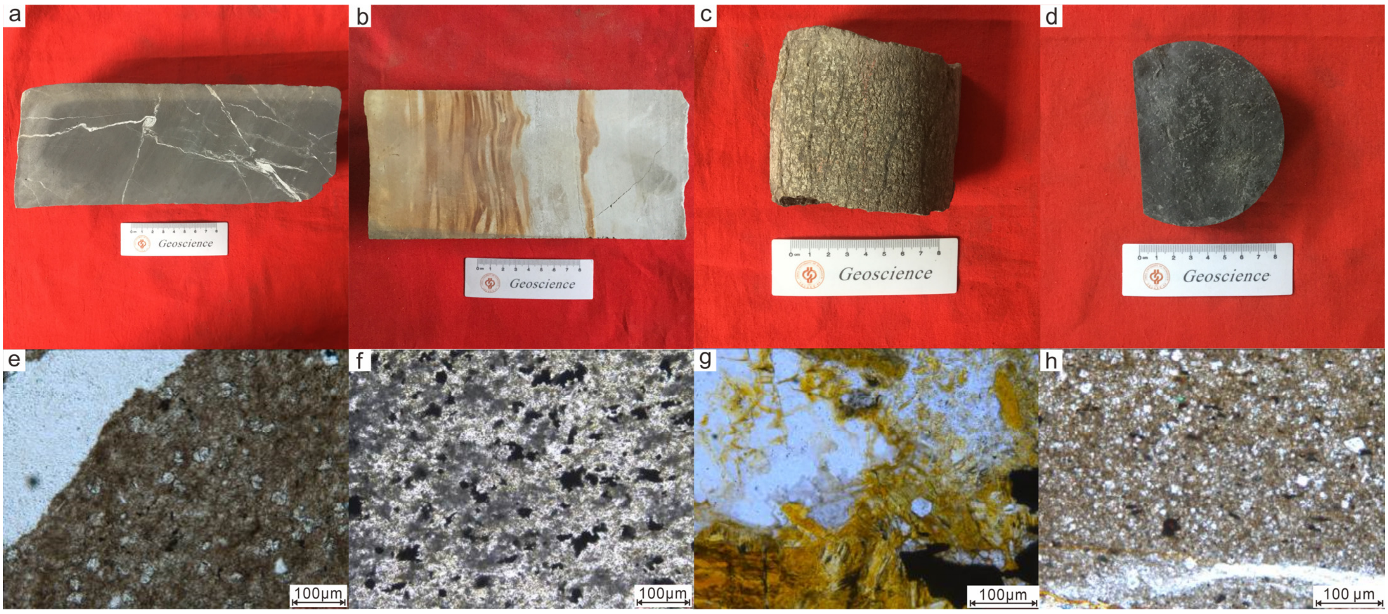

Figure 3. Core and optical microscopic characteristics of the intrusive metamorphic segment. (**a**) Well A, 1572.01–1572.25 m, black metamorphic mudstone. (**b**) Well B, 2680.41–2680.59 m, upper section of yellow-brown slate and lower section of gray-black mudstone. (**c**) Well A, 1602.35–1602.47 m, dark gray amphibolite. (**d**) Well A, 1664.83–1664.86 m, gray-black laminated sandy mudstone. (**e**) Well A, 1568.47 m, gray-black mudstone. (**f**) Well B, 2681.12 m, gray mudstone. (**g**) Well A, 1603.64 m, gray-black diabase. (**h**) Well A, 1778.73 m, gray-black argillaceous mudstone.

4.2. Pore Structure

Isotherm shapes reveal the surface properties of adsorbents, PSD, and the nature of interactions between adsorbents and adsorbates. The N_2 adsorption isotherms of the metamorphic zone samples show some variations but generally exhibit filled micropores and mono-multilayer adsorption, accompanied by capillary condensation and evaporation (Figure 5). The existence of desorption hysteresis loops was observed in each sample, indicating the surface properties, PSD, and interaction characteristics of the samples [38]. According to IUPAC recommendations (2015) [41], all sample isotherms resemble Type V isotherms, suggesting the presence of mesopores and macropores with a dominance of mesopores and capillary condensation occurring within the pores. There is a marked upward trend at $P/P_0 \geq 0.9$, while desorption curves converge with adsorption curves at $P/P_0 < 0.5$, indicating weakened capillary condensation and predominant monolayer adsorption. The isotherm adsorption curves for hornfels and diabase exhibit Type H4 hysteresis loops, implying the presence of wedge-shaped pore structures in these rocks with relatively small pore sizes and, consequently, smaller adsorption volumes. In contrast, the isotherm adsorption curves for slate and mudstone show Type H3 hysteresis loops, demonstrating that the pore structures in these rocks are mainly parallel, plate-like, and with stronger connectivity. Due to their larger pores, these rocks have relatively larger adsorption volumes.

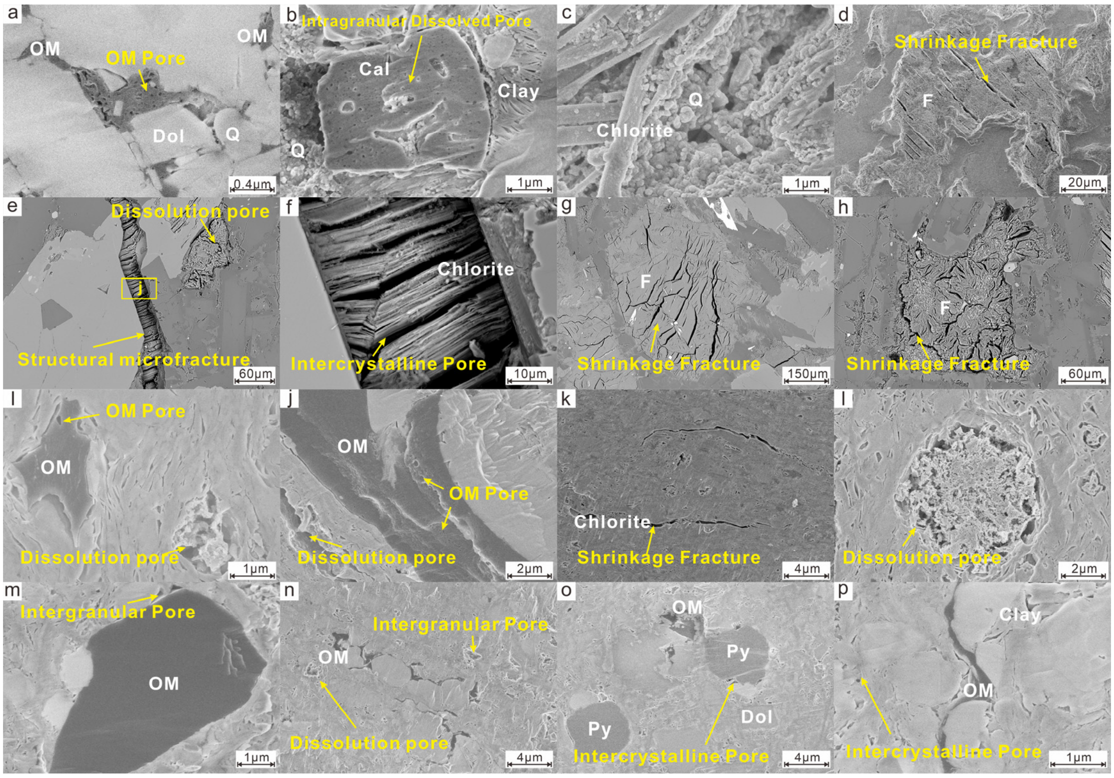

Figure 4. Pore types under SEM in the intrusive metamorphic section: (**a**) A2, 1571.87 m, organic pore development. (**b**) B2, 2681.12 m, calcite particle corrosion. (**c**) A2, 1571.87 m, chlorite and augite. (**d**) B2, 2681.12 m, shrinkage fracture. (**e**) A3, 1603.64 m, structural microfracture and calcite solution hole. (**f**) A3, 1603.64 m, chlorite-filled structure microfracture. (**g**) A3, 1603.64 m, condensation shrinkage microfracture. (**h**) A3, 1603.64 m, feldspar dissolution microfractures. (**i**) C2, 1339.78 m, small amount of OM pores. (**j**) C2, 1339.78 m, dissolution pores and OM pores. (**k**) C2, 1339.78 m, chlorite-filled shrinkage microfracture. (**l**) C2, 1339.78 m, feldspar dissolution pore. (**m**) C3, 1391.8 m, clay mineral pore and non-pore OM. (**n**) C3, 1391.8 m, intergranular pore. (**o**) C3, 1391.8 m, pyrite particles are accompanied by OM. (**p**) C3, 1391.8 m, intercrystalline pores of clay minerals. (Tips: OM: organic matter; Dol: dolomite; Cal: calcite; F: feldspar; Py: pyrite.)

The PSD of the samples from the metamorphic zones was analyzed using the DFT model based on the adsorption isotherm branches. The PSD can be described by plotting the differential pore volume (dV/dlog(D)) and the pore width. Since the area under the curve is proportional to the actual pore volume, the curve can effectively show the pore volume difference under different pore sizes [42]. The four scatter plots in the figure represent the nitrogen adsorption pore size characterization results of hornfels, diabase, slate, and mudstone, respectively. It can be obtained from the figure that the four rocks have significant differences in pore width and pore volume fraction, reflecting their different pore structure and physical properties. All samples have a peak at 4 nm, which is caused by the nitrogen adsorption experiment process. Hornfels and diabase have a small overall PSD; hornfels have multi-peak characteristics at 14 and 20–40 nm, with a peak height of about 0.04 cm^3/g possibly due to being closer to the intrusion center and being more affected by physical compression. Diabase has only a single peak at 4 nm, with no other peaks, consistent with the core and thin-section observation results, being dense and having undeveloped pores. Slate and normal mudstone have multi-peak characteristics in the PSD, with a peak height of about 0.06 cm^3/g, a larger pore volume, and more complex pore development. By comparing slate and mudstone from well A and well C, metamorphism may enhance shale's storage capacity. In addition, Table 1 lists the shale pore structure parameters obtained from N_2 adsorption experiments, including the SSA and TPV.

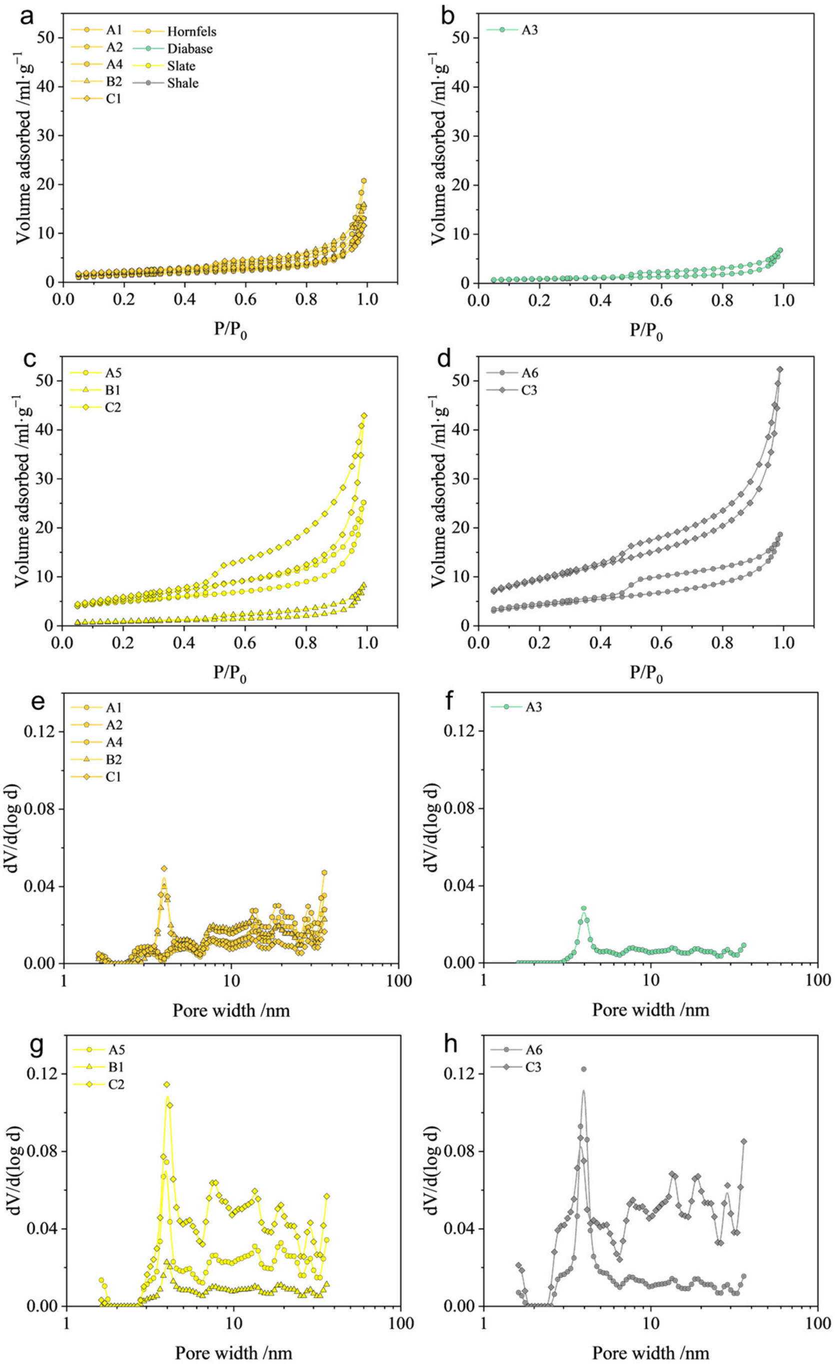

Figure 5. Nitrogen adsorption hysteresis loop in the invaded metamorphic section (**a**) Hornfels; (**b**) diabase; (**c**) slate; (**d**) shale; nitrogen adsorption PSD in the intrusive metamorphic section (**e**) Hornfels; (**f**) diabase; (**g**) slate; (**h**) shale.

4.3. Fractal Characteristics

The monofractal and multifractal characteristics of the samples from the metamorphic zones were obtained by applying the single and multifractal analysis to the isotherms of the nitrogen adsorption experiments. The nitrogen adsorption hysteresis loop was treated by the FHH monofractal model, and the observed curve presented a two-stage formula, indicating that the sample had a single fractal feature. Table 2 shows the mono-and multifractal parameters, including the monofractal dimension, the multifractal generalized dimension spectrum, and the singularity characteristic spectrum. There are few studies on metamorphic surrounding rocks and a lack of fractal analysis and comparison. The fractal results of the diabase obtained are similar to the single fractal dimension of diabase material roughness by Ji's laser scanning confocal microscope experiment [43].

Table 2. Monofractal and multifractal parameters of the intrusive metamorphic profile samples derived from N_2 adsorption.

Sample ID	Monofractal Parameters		Multifractal Parameters												
			Generalized Dimension Spectrum								Singularity Spectrum				
	D_1	D_2	D_{m0}	D_{m1}	D_{m2}	D_{m10}	$D_{m\text{-}10}$	D_{m0}– D_{m1}	$D_{m\text{-}10}$– D_{m10}	H	α_0	$\alpha_{\text{-}10}$	α_{10}	$\Delta\alpha$	R_d
A1	2.520	2.510	1.006	0.684	0.504	0.330	1.577	0.322	1.246	0.752	1.293	1.716	0.297	1.419	0.573
A2	2.559	2.464	1.006	0.730	0.554	0.369	1.510	0.276	1.141	0.777	1.249	1.644	0.332	1.312	0.522
A3	2.575	2.566	1.006	0.707	0.542	0.375	1.542	0.300	1.167	0.771	1.280	1.680	0.338	1.342	0.543
A4	2.538	2.520	1.006	0.710	0.539	0.362	1.552	0.296	1.190	0.769	1.273	1.687	0.326	1.361	0.533
A5	2.662	2.659	1.006	0.725	0.568	0.425	1.565	0.281	1.140	0.784	1.268	1.706	0.394	1.312	0.435
A6	2.724	2.514	1.006	0.815	0.665	0.490	1.454	0.192	0.964	0.833	1.174	1.585	0.449	1.136	0.313
B1	2.535	2.479	1.006	0.713	0.542	0.364	1.567	0.294	1.203	0.771	1.270	1.713	0.328	1.385	0.500
B2	2.590	2.588	1.006	0.689	0.520	0.354	1.569	0.318	1.215	0.760	1.299	1.710	0.319	1.391	0.570
C1	2.652	2.633	1.006	0.735	0.575	0.420	1.587	0.272	1.166	0.787	1.255	1.731	0.385	1.347	0.395
C2	2.595	2.505	1.006	0.735	0.569	0.394	1.523	0.272	1.129	0.785	1.248	1.663	0.355	1.308	0.479
C3	2.675	2.523	1.006	0.783	0.627	0.461	1.485	0.223	1.024	0.814	1.203	1.618	0.423	1.194	0.364

The nitrogen adsorption monofractal curve has a two-segment linear shape, and the monofractal dimensions D_1 and D_2 are obtained from the slopes of two segments (Figure 6). When $P/P_0 < 0.45$, the relative pressure is not high and N_2 molecules mostly adsorb on the pore surface as a monolayer. The slope of this segment can be used to calculate the monofractal dimension D_1, which characterizes the roughness of the pore surface. When $P/P_0 \geq 0.45$, the capillary condensation phenomenon of N_2 molecules is obvious, and the slope of this segment can be used to calculate the monofractal dimension D_2, which represents the spatial complexity of the pores. The higher the monofractal dimension of the FHH model, the stronger the heterogeneity of the pores [44,45].

If a research object has multifractal characteristics, three conditions must be met, namely that (1) $D_{m(q)}$ and $a_{(q)}$ are strictly monotonically decreasing with q; (2) $\tau_{(q)}$ and q are strictly increasing convex functions; and (3) f(a) and a are convex functions [38]. The multifractal characteristics of shale nitrogen adsorption curves indicate the irregularity and heterogeneity of the shale pore microstructure and properties at different scales. The multifractal characteristics can be characterized by a generalized dimension spectrum, singularity spectrum, mass index, and other parameters, which can be obtained by LTNA and multifractal model calculations (Figure 7). The generalized dimension $D_{m(q)}$ curve and singularity spectrum indicate that the PSD of the metamorphic zones has multifractal characteristics between 2 and 50 nm. Figure 7a shows the multifractal generalized dimension spectra of hornfels, slate, diabase, and mudstone. As q increases, $D_{m(q)}$ shows a monotonically decreasing trend, which also represents the range of PSD fluctuation probability. For uniform multifractals, the correlation curve between $D_{m(q)}$ and q is an approximate straight line. For non-uniform multifractals, they show a decreasing function transition trend. The steeper the relationship curve between $D_{m(q)}$ and q, the wider the range of $D_{m(q)}$, that is, the larger the distribution range of different singularity intensity multifractal structures, the greater the heterogeneity of multifractal structures. D_{m0} is considered as the capacity dimension or box dimension. The values of all samples are 1.006, indicating the multifractal measurement of non-empty boxes with a density probability at different scales. If the mass or porosity of any box is not zero, the value of Dm_0 will be equal to 1 [46]. The value range of the information dimension D_{m1} is 0.684~0.815, which is usually considered to evaluate the local concentration degree and pore interval of PSD. The range of correlation dimension D_{m2} is 0.504~0.665, which reflects the characteristics of the second sampling moment [47]. Generally speaking, the larger the multifractal dimension, the more complex the pore structure characterized, the larger the spectral width, and the more obvious the multifractal characteristics. D_{m-10} ranges from 1.454 to 1.587, and D_{m10} ranges from 0.330 to 0.490. The spectral width (D_{m-10}–D_{m10}) ranges from 0.964 to 1.246. The range of the H value is 0.752~0.833, and the average value is 0.782. The singularity spectrum can also describe the multifractal characteristics (Figure 7b). The singularity spectra of all samples are convex parabolic. The singularity index α_0 of the samples ranges from 1.174 to 1.299, and the average value is 1.256. Generally speaking, the $\Delta\alpha$ values were lower in the samples with a wider PSD and higher gas adsorption capacity. For example, sample A6 has the smallest $\Delta\alpha$ value of 1.136, indicating that its PSD is most uniform; for example, samples with obvious double-peak PSD and a lower gas adsorption volume have higher $\Delta\alpha$ values. The PSD heterogeneity of sample A1 is the strongest, and the $\Delta\alpha$ value can reach up to 1.419, which is closely related to the PSD characteristics. For PSD caused by intrusion metamorphism, the peak width is narrower, the peak height is higher, and $\Delta\alpha$ is larger. The cross-sections of the left curves of singularity spectra are wider and longer than those of right curves relative to symmetric lines. The singular spectrum lines reflect regions where the probability density of pore volume distribution is relatively high (concentrated) and low (sparse) on both sides of the symmetry line, respectively. The R_d values of all samples are positive, indicating that sparse areas dominate in pore volume distribution in these samples.

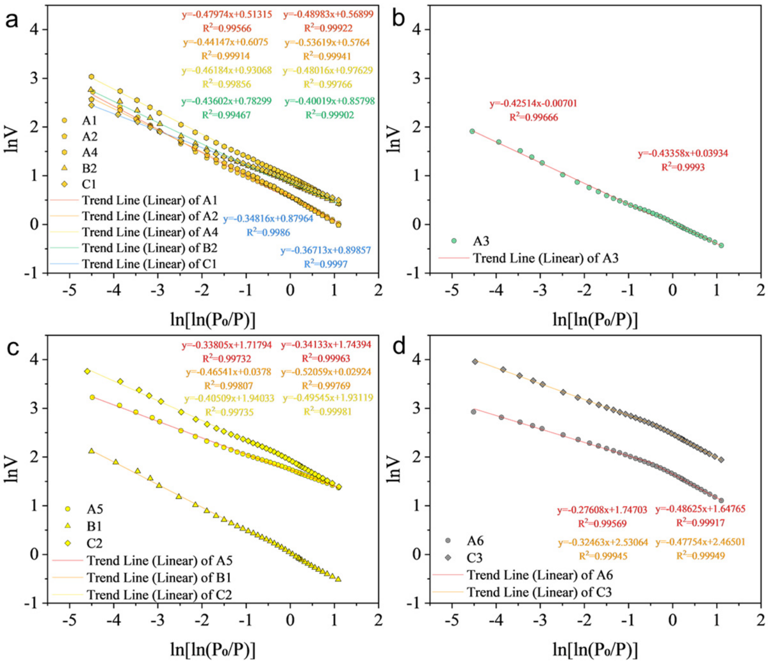

Figure 6. Fractal characteristics and fractal dimensions of nitrogen adsorption in the intrusive metamorphic section. (**a**) Hornfels; (**b**) diabase; (**c**) slate; (**d**) shale.

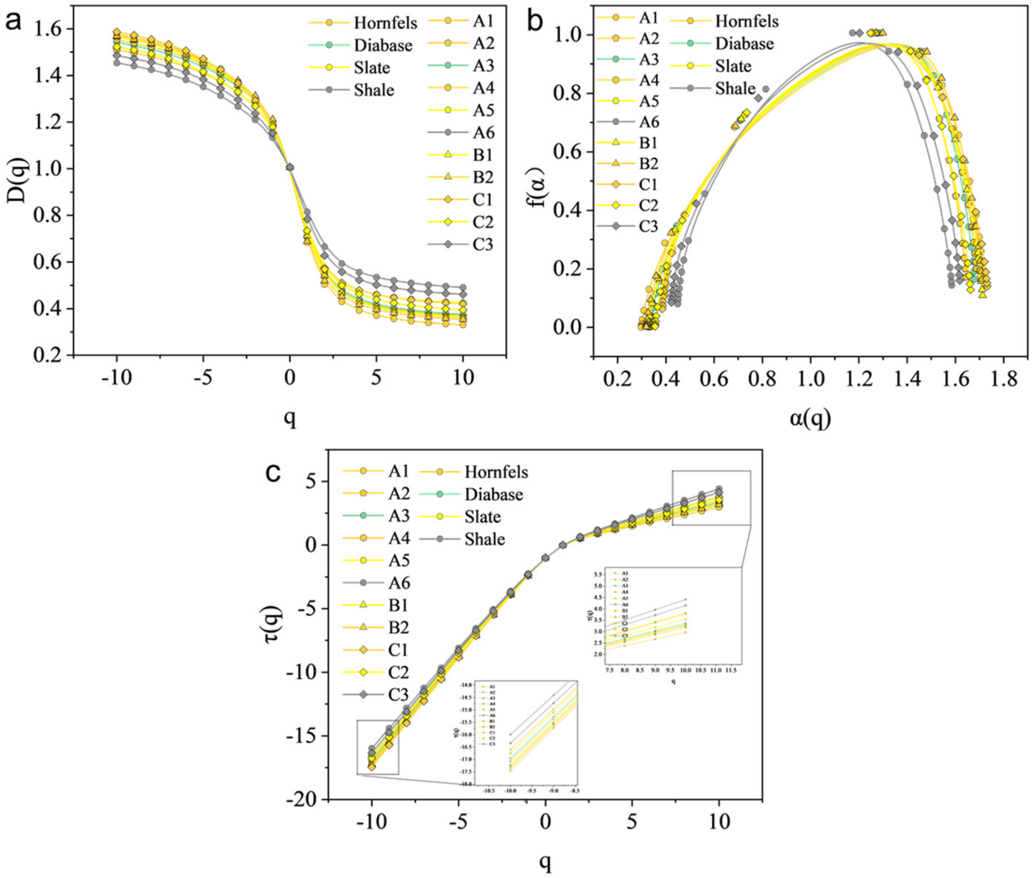

Figure 7. Multifractal generalized dimension spectrum, singular feature spectrum (**a**), mass index feature (**b**), and multifractal parameter feature (**c**) of intrusive metamorphic section.

5. Discussion

5.1. Differences Between Diabase Intrusive and Non-Intrusive Shale Reservoirs

5.1.1. Difference In Monofractal and Multifractal Behaviors Between Metamorphic Shale and Normal Shale

The pore type and size of the shale in metamorphic zones are significantly different and heterogeneous due to the influence of intrusion metamorphism. This research selected the well A samples with intact cores from the metamorphic zones for separate discussion, avoiding the effect of compaction at different depths. As shown in Figure 8, the monofractal dimensions D_1 and D_2 of the intrusion zone show a general trend of decreasing first and then increasing from the intrusion center to the normal shale zone, while the monofractal dimension D_2 of the normal shale is lower, indicating that the pore surface of the normal shale is rough and the complexity of the pore space is lower than that of the intrusion center zone. This may be due to the combined effect of mechanical compression, dissolution, and baking on the metamorphic zone [48].

The multifractal parameters can further analyze the pore morphology characteristics of the upper and lower metamorphic zones. As shown in Figure 8, the H index gradually decreases from the lower normal shale to the upper metamorphic zone hornfels, while $\Delta\alpha$ gradually increases from the lower to the upper metamorphic zone hornfels, indicating that the pore connectivity of the upper metamorphic zone is poor and the pore heterogeneity is strong. R_d values are all positive, showing that the PSD is mainly controlled by sparse pores [38,49].

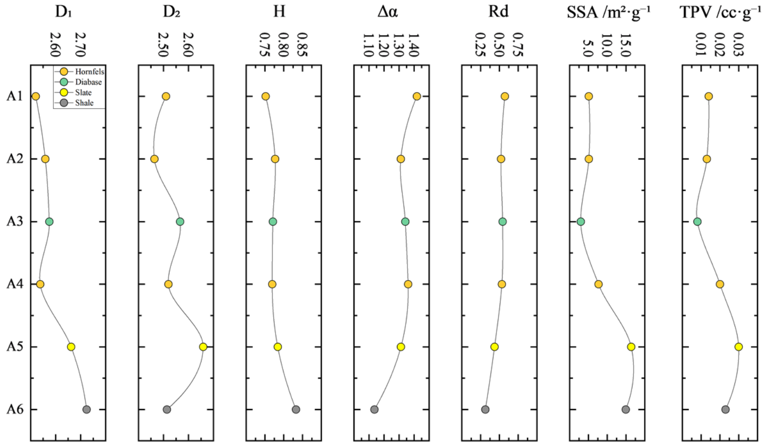

Figure 8. Variation characteristics of fractal and pore structure parameters of surrounding rocks in intrusive metamorphic section.

The nitrogen adsorption parameters also confirm the above inference. From the intrusion center to the normal shale zone, the SSA and TPV increase gradually, and the pore structure of the lower metamorphic zone, especially the slate metamorphic zone, is better.

5.1.2. Impact of Geochemical Features

The intrusion of high-temperature and high-pressure diabase can change the geochemical properties of surrounding rocks, such as organic abundance and maturity. The cross-plot of pore structure monofractal parameters (D_1 and D_2), multifractal parameters ($\Delta\alpha$ and H), and geochemical parameters (TOC and R_o) (Figure 9) were drawn to reveal the influence of geochemical properties on pore heterogeneity. With the increase in TOC content, the monofractal parameters of the metamorphic zone decreased, indicating a slight decrease in pore surface roughness and spatial complexity. TOC had no significant impact on the multifractal parameters of the metamorphic zone. R_o variation had an obvious effect on the monofractal characteristics of the shale pore structure. Affected by the high-temperature intrusion, the Ro value of the low-maturity shale layer increased gradually towards the intrusion center [50] and both D_1 and D_2 decreased, indicating a decrease in pore surface roughness and spatial complexity. The multifractal dimension $\Delta\alpha$ increased, while the H index decreased, indicating an increase in pore heterogeneity and a decrease in connectivity. The compression effect of diabase on the surrounding rocks caused deformation and compaction of the surrounding rocks, mineral orientation, and filling or deformation of the original pores, resulting in a reduction in pore space and a decrease in pore surface roughness. At the same time, the compaction of the surrounding rocks also increased the density of the rocks and reduced the connectivity of the pores. The high temperature brought about by the intrusion promoted the OM to generate hydrocarbons in the surrounding rocks, forming OM pores in shale. The organic acids produced could further dissolve mineral particles to form secondary dissolution pores and affect the morphology of the pore surface, enhancing shale pore heterogeneity [51]. The closer to the intrusion center, the stronger the mechanical compaction effect and the higher the R_o value. Therefore, it showed that with the increase in R_o, pore surface roughness and connectivity decreased and heterogeneity increased.

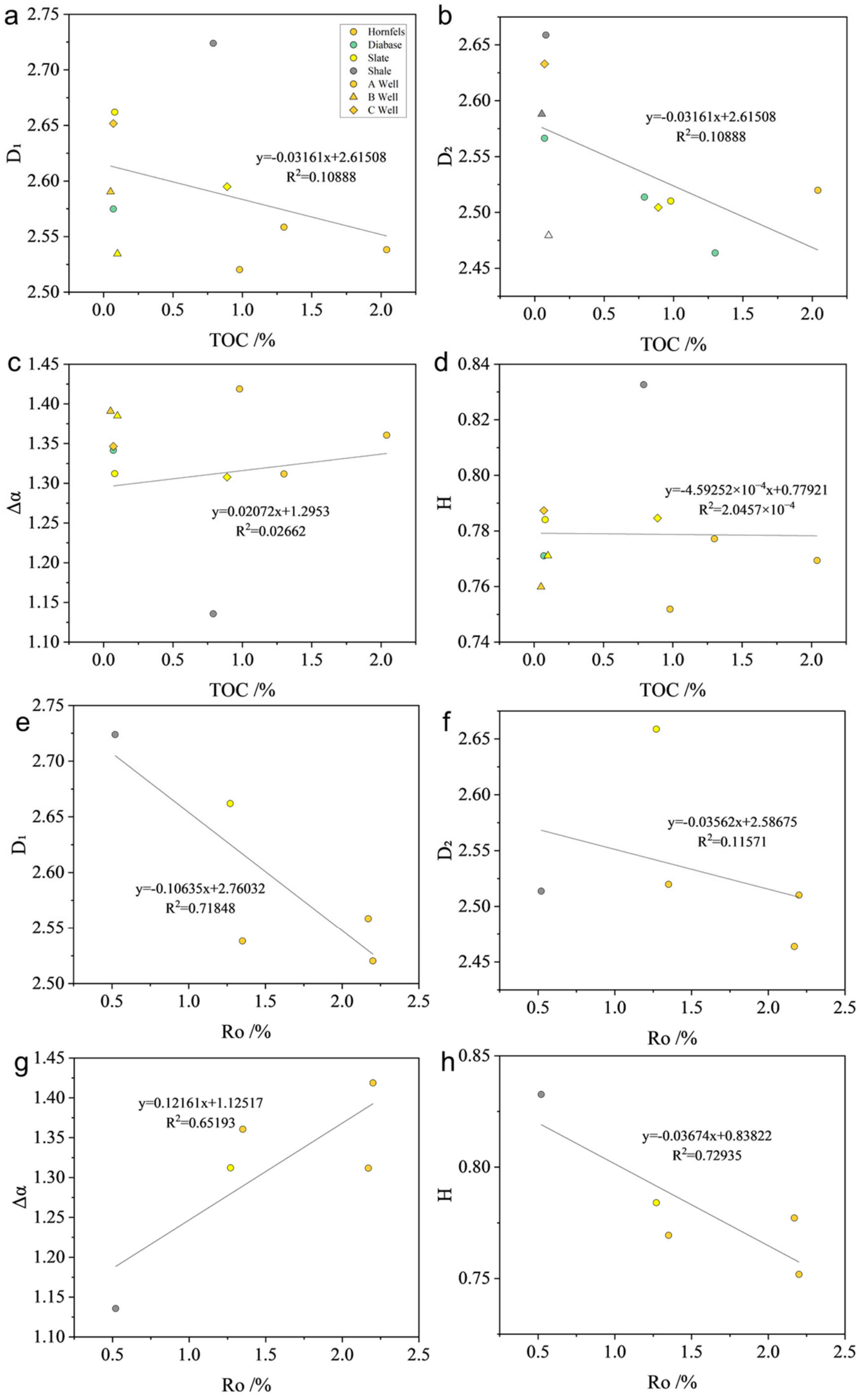

Figure 9. The impact on pore structure heterogeneity of the intrusive metamorphic profile samples from organic geochemical characteristics. (**a**,**b**) D_1 and D_2 vs. TOC; (**c**,**d**) $\Delta\alpha$ and H vs. TOC; (**e**,**f**) D_1 and D_2 vs. R_o; (**g**,**h**) $\Delta\alpha$ and H vs. R_o.

5.1.3. Impact of Pore Volume on Pore Heterogeneity

Figure 10 shows the correlations between D_1, D_2, $\Delta\alpha$, and H and the SSA and TPV. The SSA and TPV have some influence on the monofractal dimension D_1, showing a weak positive correlation (Figure 10a,e), but no obvious correlation with D_2 (Figure 10b,f). For the multifractal parameters $\Delta\alpha$ and the H index, $\Delta\alpha$ decreases as the SSA and TPV increase (Figure 10c,g), while the H index shows the opposite correlation (Figure 10d,h). The increase in the SSA and TPV reduces the heterogeneity of shale pores in the metamorphic zone and increases the surface roughness and connectivity of pores.

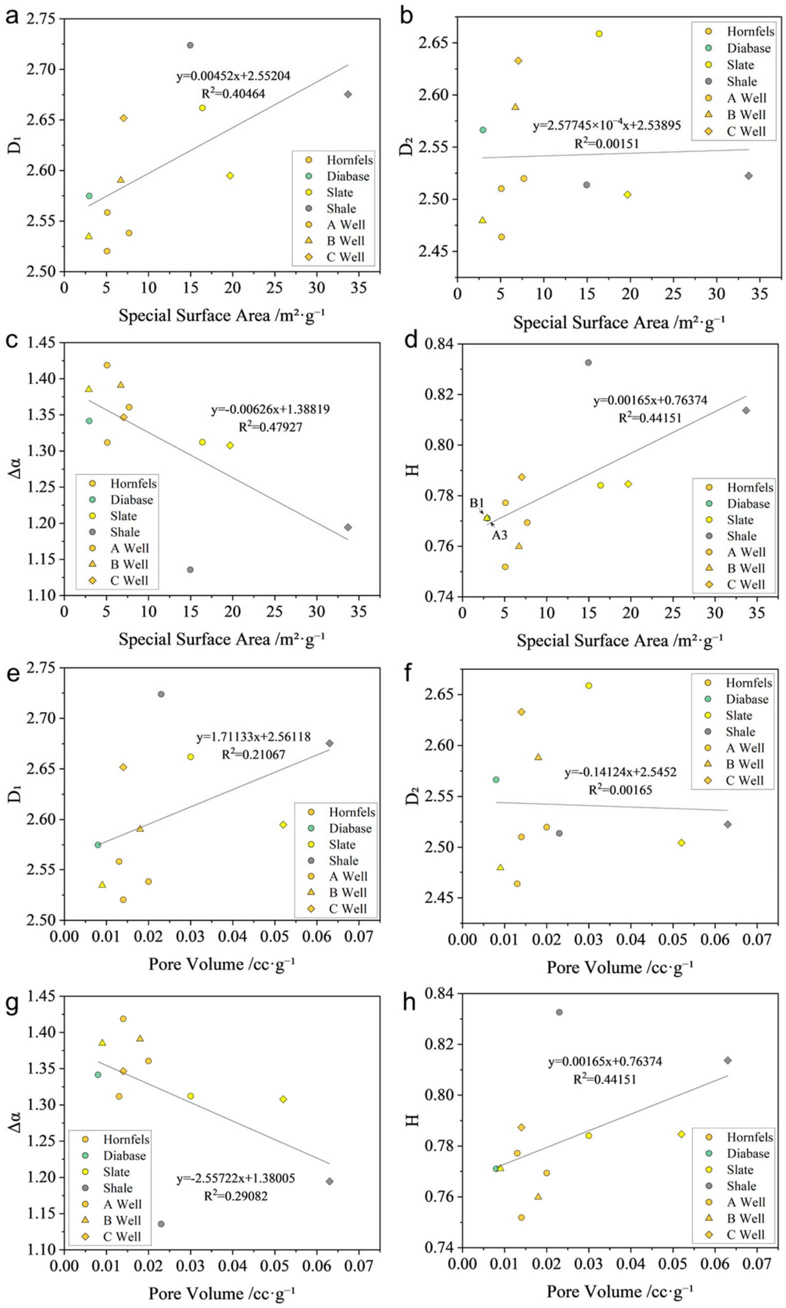

Figure 10. Intersection diagram of monofractal and multifractal parameters with SSA and pore volume of intrusive metamorphic zone. (**a**,**b**) D_1 and D_2 vs. SSA; (**c**,**d**) $\Delta\alpha$ and H vs. SSA; (**e**,**f**) D_1 and D_2 vs. TPV; (**g**,**h**) $\Delta\alpha$ and H vs. TPV.

5.2. Influence Mechanism of Diabase Intrusion on Shale Reservoir

5.2.1. Physical Effect

The intrusion of diabase into shale caused a significant amount of kinetic energy to compress the surrounding rocks [52,53]. The nearby shale dehydrated due to metamorphism, became more brittle, and fractured under mechanical compression (Figure 4k), forming numerous microcracks. Mineral particles showed orientation characteristics in the high-energy environment, and the pore direction tended to be consistent (Figure 4d).

5.2.2. Thermal Effect

In the initial phase of the intrusion process, the large temperature difference between the central rock mass and surrounding rocks caused the fluid in mudstone to expand, generating stress concentration and resulting in cracks or an extension of existing cracks in the reservoir. The high temperature makes the OM of low-maturity shale generate hydrocarbons, promote the formation of OM pores, and further enhance the heterogeneity of pores in the metamorphic zone. After the intrusion rock cooled, its volume shrank, causing the surrounding mudstone to be subjected to tensile stress [54]. Coaxial tensile microcracks were visible in the hornfels metamorphic zone and slate metamorphic zone (Figure 3a,b). The LTNA hysteresis loop showed that the samples from the hornfels zone closest to the intrusion were mostly wedge-shaped narrow slit pores (Figure 5a,c), which further confirmed the existence of a large number of microcracks.

5.2.3. Chemical Effect

The hydrothermal fluid brought about by diabase intrusion and the acidic fluid from the hydrocarbon generation of OM reacted with the surrounding rocks in a water–rock interaction, dissolving or precipitating some minerals, such as calcite dissolution, quartz recrystallization, pyrite formation, and clay mineral transformation, forming new pores or changing the original pore morphology [13,55–58]. At the same time, it changed the chemical composition and physical properties of the surrounding rocks, producing new mineral phases, such as rhodochrosite, garnet, diopside, and other minerals. These processes increased the porosity and permeability, enhancing the storage capacity of the surrounding rocks, which was beneficial for oil and gas accumulation.

5.2.4. Transformation Model of Shale Micropores by Diabase Intrusion

The intrusion of diabase into shale surrounding rocks mainly underwent two stages of transformation. In the first stage, due to the continuous compression effect of high-temperature rock mass, mechanical fractures occurred in the surrounding rocks, which caused mineral orientation in the surrounding rocks and formed a large number of microcracks. Due to the intrusion of high-temperature rock mass, high-temperature baking occurred in the surrounding rocks, which caused a metamorphism of minerals in the surrounding rocks, making them brittle. The intrusion also brought stratum water, which could promote the hydrocarbon generation of OM under high temperature. These generated hydrocarbons filled in the surrounding rocks to form some OM pores and secondary dissolution pores (Figure 11a,b).

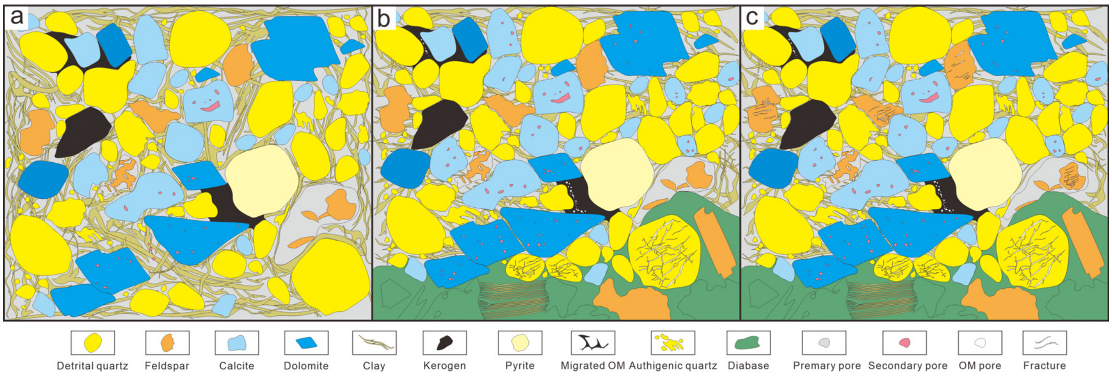

Figure 11. Micropore evolution model of diabase intrusion metamorphic zone. (**a**) Schematic diagram of shale particles and pores before diabase intrusion after sedimentary diagenesis; (**b**) schematic diagram of influence of diabase on mineral particles and pores in early stage of intrusion; (**c**) schematic diagram of mineral particles and pores from end of intrusion to end of metamorphism.

After entering the second stage, the high-temperature rock mass began to cool down, causing a cooling shrinkage of rock mass. This cooling shrinkage process produced some condensation shrinkage cracks. These condensation cracks were wider and deeper than microcracks, and they developed along the fractures and cracks of the rock mass. These condensation cracks were usually filled with minerals such as chlorite, and the formation of fillers gave condensation cracks a certain stability (Figure 11c).

Through these two stages in the process, diabase intrusion into shale surrounding rock produced significant transformation effects on surrounding rocks. Mechanical fracture, mineral orientation, OM pores, secondary dissolution pores, and condensation shrinkage cracks provided important mechanisms for the changes in and evolution of properties and structure of surrounding rocks. These transformation effects had some impact on the physical and chemical properties of shale, which then affected the storage capacity and fluid migration ability of reservoirs.

5.3. Petroleum Geological Significance of Shale Pore Change Caused by Diabase Intrusion and Transformation

The changes in the shale pore structure observed due to diabase intrusion have a profound impact on oil and gas recovery in practical applications. Diabase intrusion usually leads to a thermal alteration and mechanical deformation of the surrounding shale matrix. In terms of heat, intrusion will lead to an increase in temperature, which may cause the thermal maturation of organic matter and enhance the conversion of kerogen to hydrocarbons. In mechanics, intrusion can induce the formation of new fractures and modify the existing pore network, thereby increasing the permeability and porosity of shale. These changes can significantly improve the connectivity between pores, enhance fluid flow, and make hydrocarbons more easily extracted. However, the extent and nature of these impacts are highly variable and depend on several key factors. These include the temperature and duration of thermal exposure, the chemical and physical composition of diabase, and the initial properties of shale. For example, higher temperatures and longer exposure times can lead to more extensive thermal maturation and pore network modification, while the presence of certain minerals in diabase can affect the mechanical properties of shale.

By addressing these research areas, a more comprehensive understanding of the interactions between diabase intrusion and shale pore structure can be found, ultimately leading to more effective and efficient hydrocarbon recovery practices.

6. Conclusions

Based on the above study of the transformation of a shale pore structure by diabase intrusion, the following conclusions can be drawn:

(1) The shale after diabase intrusion transformation shows stronger pore heterogeneity than normal shale but lower pore roughness. The pore connectivity of the upper metamorphic zone is poor and the pore heterogeneity is strong, while the lower metamorphic zone has a better pore structure.

(2) OM abundance has no obvious effect on the pore structure of the metamorphic zone, while R_o variation has a significant impact on the fractal characteristics of shale pores. Pore volume also affects pore heterogeneity. Larger SSA and TPV have lower pore heterogeneity as well as higher surface roughness and pore connectivity.

(3) The transformation of shale surrounding rocks by diabase intrusion is mainly influenced by three factors, namely mechanical compression, the thermal effect, and chemical effect. In terms of mechanical compression, the intrusion effect of diabase causes fracture and microcrack formation in the surrounding rocks, leading to increased pore heterogeneity. In terms of the thermal effect, high temperatures promoted the hydrocarbon generation of OM and pore formation, and the condensation shrinkage cracks produced by the cooling process also affected the pore structure. In terms of the chemical effect, the hydrothermal fluid of the intrusion zone reacts with the surrounding rocks, dissolves or precipitates minerals, forms new pores, and changes the pore structure.

(4) A transformation model of shale micropores by diabase intrusion was established. Diabase intrusion into shale surrounding rocks produces an important transformation of the properties and structure of surrounding rocks through mechanical fracture, min-

eral orientation, OM pores, secondary dissolution pores, and condensation shrinkage cracks. These transformation effects have a significant impact on the pore structure of shale reservoirs, affecting their storage performance.

Author Contributions: Conceptualization, X.L.; methodology, W.X.; formal analysis, B.S. and T.L.; investigation, Y.Z. and W.P.; data curation, Q.L., H.D. and S.L.; writing—original draft, Z.H. All authors have read and agreed to the published version of the manuscript.

Funding: The study was financially supported by the National Natural Science Foundation of China (grant No.42072150).

Data Availability Statement: No new data were created or analyzed in this study.

Acknowledgments: We would like to extend our sincere appreciation to the SINOPEC Jiangsu Oilfield Company for generously providing us with samples and data. We acknowledge Thanakorn Prasansri and three anonymous reviewers for their valuable comments and suggestions, which greatly improved the manuscript from an earlier version.

Conflicts of Interest: The authors declare that they have no known competing financial interests or personal relationships that could have appeared to influence the work reported in this paper.

References

1. Jin, Z. Several Issues Worthy of Attention in Current Lacustrine Shale Oil Exploration and Development. *Pet. Explor. Dev.* **2021**, *14*, 1471–1484. [CrossRef]
2. Rong, H.; Jiao, Y.; Wu, L.; Zhao, X.; Cao, M.; Liu, W. Effects of Igneous Intrusions on Diagenesis and Reservoir Quality of Sandstone in the Songliao Basin, China. *Mar. Pet. Geol.* **2021**, *127*, 104980. [CrossRef]
3. Olavsdottir, J.; Andersen, M.S.; Boldreel, L.O. Reservior Quality of Intrabasalt Volcaniclastic Units Onshore Faroe Islands, North Atlantic Igneous Province, Northeast Atlantic. *Bulletin* **2015**, *99*, 467–497. [CrossRef]
4. Wei, W.; Azmy, K.; Zhu, X. Impact of Diagenesis on Reservoir Quality of the Lacustrine Mixed Carbonate-Siliciclastic-Volcaniclastic Rocks in China. *J. Asian Earth Sci.* **2022**, *233*, 105265. [CrossRef]
5. Wang, K.; Liu, H.; Ren, W.; Li, W.; Yu, Z. Influence of Cenozoic Diabase Intrusion on Reservoir Properties of Mudstone Wallrocks in the Yangxin Sub-depression, Subei Basin. *Geoscience* **2022**, *36*, 1563–1573. [CrossRef]
6. Liu, C.; Xie, Q.; Wang, G.; Zhang, C.; Wang, L.; Qi, K. Reservoir Properties and Controlling Factors of Contact Metamorphic Zones of the Diabase in the Northern Slope of the Gaoyou Sag, Subei Basin, Eastern China. *J. Nat. Gas Sci. Eng.* **2016**, *35*, 392–411. [CrossRef]
7. Simonet, B.R.T.; Brenner, S.; Peters, K.E.; Kaplan, I.R. Thermal Alteration of Cretaceous Black Shale by Diabase Intrusions in the Eastern Atlantic—II. Effects on Bitumen and Kerogen. *Geochim. Cosmochim. Acta* **1981**, *45*, 1581–1602. [CrossRef]
8. Sun, B.; Liu, X.; Liu, J.; Liu, Q.; Duan, H.; Liu, S.; Guan, M.; Liu, T.; Hua, Z.; Sheng, K.; et al. Lacustrine Shale Oiliness Influenced by Diabase Intrusions in the Paleogene Funing Formation, Subei Basin, China. *Pet. Sci.* **2023**. [CrossRef]
9. Liu, C.; Gu, L.; Wang, J.; Si, S. Reservoir Characteristics and Forming Controls of Intrusive-Metamorphic Reservoir Complex: A Case Study on the Diabase-Metamudstone Rocks in the Gaoyou Sag, Eastern China. *J. Pet. Sci. Eng.* **2019**, *173*, 705–714. [CrossRef]
10. Dow, W.G. Kerogen Studies and Geological Interpretations. *J. Geochem. Explor.* **1977**, *7*, 79–99. [CrossRef]
11. Leif, R.N.; Simoneit, B.R.T. Ketones in Hydrothermal Petroleums and Sediment Extracts from Guaymas Basin, Gulf of California. *Org. Geochem.* **1995**, *23*, 889–904. [CrossRef]
12. Lenz, R.L.; da Silva, T.F.; González, M.B.; Barrionuevo, S.; Kalkreuth, W. Behavior of Molecular Maturity Parameters in Overmature Shales Affected by Diabase Intrusion (Irati Formation, Paraná Basin—Brazil). *Int. J. Coal Geol.* **2023**, *272*, 104264. [CrossRef]
13. Summer, N.S.; Ayalon, A. Dike Intrusion into Unconsolidated Sandstone and the Development of Quartzite Contact Zones. *J. Struct. Geol.* **1995**, *17*, 997–1010. [CrossRef]
14. Schwartz, B.; Huffman, K.; Thornton, D.; Elsworth, D. The Effects of Mineral Distribution, Pore Geometry, and Pore Density on Permeability Evolution in Gas Shales. *Fuel* **2019**, *257*, 116005. [CrossRef]
15. Liu, X.; Lai, J.; Fan, X.; Shu, H.; Wang, G.; Ma, X.; Liu, M.; Guan, M.; Luo, Y. Insights in the Pore Structure, Fluid Mobility and Oiliness in Oil Shales of Paleogene Funing Formation in Subei Basin, China. *Mar. Pet. Geol.* **2020**, *114*, 104228. [CrossRef]
16. Duan, R.; Xu, Z.; Dong, Y.; Liu, W. Characterization and Classification of Pore Structures in Deeply Buried Carbonate Rocks Based on Mono- and Multifractal Methods. *J. Pet. Sci. Eng.* **2021**, *203*, 108606. [CrossRef]
17. Othman, R.; Arouri, K.R.; Ward, C.R.; McKirdy, D.M. Oil Generation by Igneous Intrusions in the Northern Gunnedah Basin, Australia. *Org. Geochem.* **2001**, *32*, 1219–1232. [CrossRef]
18. Goodarzi, F.; Gentzis, T.; Dewing, K. Influence of Igneous Intrusions on the Thermal Maturity of Organic Matter in the Sverdrup Basin, Arctic Canada. *Int. J. Coal Geol.* **2019**, *213*, 103280. [CrossRef]
19. Sun, B.; Liu, X.; Liu, J.; Wang, G.; Shu, H.; Luo, Y.; Liu, T.; Hua, Z. The Heterogeneity of Lithofacies Types, Combination Modes, and Sedimentary Model of Lacustrine Shale Restricted by High-frequency Sequence. *Geol. J.* **2022**, *57*, 4035–4051. [CrossRef]

20. Hua, Z.; Liu, X.; Sun, B.; Liu, T.; Liu, J.; Liu, Q.; Liu, S.; Bi, T. Differences in Oil and Gas Enrichment in Slope Belts of Rift Basins and Main Controlling Factors for Hydrocarbon Accumulation: A Case Study of Sanhe Sub-Sag in Jinhu Sag, Subei Basin. *Pet. Geol. Exp.* **2022**, *44*, 950–958. [CrossRef]
21. Mao, F. Determination of the Forming Time of Diabase in the Northern Slope of Gaoyou Sag and It' s Relationship with Oil and Gas. *Pet. Explor. Dev.* **2000**, *27*, 19-20+16-15+7.
22. Shaodong, Y.E.; Hongmin, R.E.; Chuhua, L.I. The Distribution of Cenozoic Intrusive Rocks in the North Jiangsu Basin andIts Geological Significances. *Geol. Rev.* **2010**, *56*, 269–274. [CrossRef]
23. Guan, M.; Liu, X.; Jin, Z.; Lai, J.; Sun, B.; Zhang, P.; Chen, K. The Evolution of Pore Structure Heterogeneity during Thermal Maturation in Lacustrine Shale Pyrolysis. *J. Anal. Appl. Pyrolysis* **2022**, *163*, 105501. [CrossRef]
24. Aljamaan, H.; Al Ismail, M.; Kovscek, A.R. Experimental Investigation and Grand Canonical Monte Carlo Simulation of Gas Shale Adsorption from the Macro to the Nano Scale. *J. Nat. Gas Sci. Eng.* **2017**, *48*, 119–137. [CrossRef]
25. Fink, R.; Amann-Hildenbrand, A.; Bertier, P.; Littke, R. Pore Structure, Gas Storage and Matrix Transport Characteristics of Lacustrine Newark Shale. *Mar. Pet. Geol.* **2018**, *97*, 525–539. [CrossRef]
26. Jiang, J.; Yang, W.; Cheng, Y.; Zhao, K.; Zheng, S. Pore Structure Characterization of Coal Particles via MIP, N_2 and CO_2 Adsorption: Effect of Coalification on Nanopores Evolution. *Powder Technol.* **2019**, *354*, 136–148. [CrossRef]
27. Han, W.; Zhou, G.; Gao, D.; Zhang, Z.; Wei, Z.; Wang, H.; Yang, H. Experimental Analysis of the Pore Structure and Fractal Characteristics of Different Metamorphic Coal Based on Mercury Intrusion-nitrogen Adsorption Porosimetry. *Powder Technol.* **2020**, *362*, 386–398. [CrossRef]
28. Zhang, S.; Tang, S.; Tang, D.; Huang, W.; Pan, Z. Determining Fractal Dimensions of Coal Pores by FHH Model: Problems and Effects. *J. Nat. Gas Sci. Eng.* **2014**, *21*, 929–939. [CrossRef]
29. Russell, D.A.; Hanson, J.D.; Ott, E. Dimension of Strange Attractors. *Phys. Rev. Lett.* **1980**, *45*, 1175–1178. [CrossRef]
30. Chaudhuri, B.B.; Sarkar, N. Texture Segmentation Using Fractal Dimension. *IEEE Trans. Pattern Anal. Mach. Intell.* **1995**, *17*, 72–77. [CrossRef]
31. Ferreiro, J.P.; Wilson, M.; Vázquez, E.V. Multifractal Description of Nitrogen Adsorption Isotherms. *Vadose Zone J.* **2009**, *8*, 209–219. [CrossRef]
32. Halsey, T.C.; Jensen, M.H.; Kadanoff, L.P.; Procaccia, I.; Shraiman, B.I. Fractal Measures and Their Singularities: The Characterization of Strange Sets. *Phys. Rev. A* **1986**, *33*, 1141–1151. [CrossRef]
33. Chhabra, A.; Jensen, R.V. Direct Determination of the f(α) Singularity Spectrum. *Phys. Rev. Lett.* **1989**, *62*, 1327–1330. [CrossRef] [PubMed]
34. San José Martínez, F.; Martín, M.A.; Caniego, F.J.; Tuller, M.; Guber, A.; Pachepsky, Y.; García-Gutiérrez, C. Multifractal Analysis of Discretized X-Ray CT Images for the Characterization of Soil Macropore Structures. *Geoderma* **2010**, *156*, 32–42. [CrossRef]
35. Grassberger, P. Generalized Dimensions of Strange Attractors. *Phys. Lett. A* **1983**, *97*, 227–230. [CrossRef]
36. Riedi, R.H.; Crouse, M.S.; Ribeiro, V.J.; Baraniuk, R.G. A Multifractal Wavelet Model with Application to Network Traffic. *IEEE Trans. Inform. Theory* **1999**, *45*, 992–1018. [CrossRef]
37. Liu, K.; Ostadhassan, M.; Zou, J.; Gentzis, T.; Rezaee, R.; Bubach, B.; Carvajal-Ortiz, H. Multifractal Analysis of Gas Adsorption Isotherms for Pore Structure Characterization of the Bakken Shale. *Fuel* **2018**, *219*, 296–311. [CrossRef]
38. Guan, M.; Liu, X.; Jin, Z.; Lai, J. The Heterogeneity of Pore Structure in Lacustrine Shales: Insights from Multifractal Analysis Using N_2 Adsorption and Mercury Intrusion. *Mar. Pet. Geol.* **2020**, *114*, 104150. [CrossRef]
39. Wang, Y.; Cheng, H.; Qinhong, H.; Liu, L.; Jia, L.; Gao, S.; Wang, Y. Pore Structure Heterogeneity of Wufeng-Longmaxi Shale, Sichuan Basin, China: Evidence from Gas Physisorption and Multifractal Geometries. *J. Pet. Sci. Eng.* **2021**, *208*, 109313. [CrossRef]
40. Zhao, P.; Wang, X.; Cai, J.; Luo, M.; Zhang, J.; Liu, Y.; Rabiei, M.; Li, C. Multifractal Analysis of Pore Structure of Middle Bakken Formation Using Low Temperature N_2 Adsorption and NMR Measurements. *J. Pet. Sci. Eng.* **2019**, *176*, 312–320. [CrossRef]
41. Song, X.; Zhou, X.; Lv, X. Quantitative Evaluation of Pore Connectivity of Shales with a Type H3 Sorption Hysteresis Loop. *J. Asian Earth Sci.* **2023**, *247*, 105595. [CrossRef]
42. Clarkson, C.R.; Solano, N.; Bustin, R.M.; Bustin, A.M.M.; Chalmers, G.R.L.; He, L.; Melnichenko, Y.B.; Radliński, A.P.; Blach, T.P. Pore Structure Characterization of North American Shale Gas Reservoirs Using USANS/SANS, Gas Adsorption, and Mercury Intrusion. *Fuel* **2013**, *103*, 606–616. [CrossRef]
43. Ji, X.; Chen, Y.; Hou, Y.; Dai, C.; Chen, B.; Zou, H. Surface Microscopic Properties of Various Aggregates Using Laser Scanning Confocal Microscope. *Constr. Build. Mater.* **2021**, *290*, 123222. [CrossRef]
44. Wang, J.; Cao, Y.; Liu, K.; Gao, Y.; Qin, Z. Fractal Characteristics of the Pore Structures of Fine-Grained, Mixed Sedimentary Rocks from the Jimsar Sag, Junggar Basin: Implications for Lacustrine Tight Oil Accumulations. *J. Pet. Sci. Eng.* **2019**, *182*, 106363. [CrossRef]
45. Liu, X.; Jin, Z.; Lai, J.; Fan, X.; Guan, M.; Shu, H.; Wang, G.; Liu, M.; Luo, Y. Fractal Behaviors of NMR Saturated and Centrifugal T2 Spectra in Oil Shale Reservoirs: The Paleogene Funing Formation in Subei Basin, China. *Mar. Pet. Geol.* **2021**, *129*, 105069. [CrossRef]
46. Caniego, F.J.; Martí, M.A.; San José, F. Rényi Dimensions of Soil Pore Size Distribution. *Geoderma* **2003**, *112*, 205–216. [CrossRef]
47. Vázquez, E.V.; Ferreiro, J.P.; Miranda, J.G.V.; González, A.P. Multifractal Analysis of Pore Size Distributions as Affected by Simulated Rainfall. *Vadose Zone J.* **2008**, *7*, 500–511. [CrossRef]

48. Bicca, M.M.; Kalkreuth, W.; Rosa, A.L.; Simão, G.; Levandowski, J.; Silva, T.F.; Anzolin, H.M. Effect of Diabase Intrusion on the CBM-Bearing Coalfields of Southern Brazil: A Review. *J. S. Am. Earth Sci.* **2022**, *119*, 104041. [CrossRef]
49. Miao, Z.; Qiu, Z.; Guofu, L.; Xuehai, F.; Chaochao, D.; Huihu, L.; Hongjie, X. Fluid Distribution and Pore Structure Multifractal Characteristics Analysis of Coal Measure Mudstone. *J. Nat. Gas Sci. Eng.* **2021**, *88*, 103810. [CrossRef]
50. Martins, C.M.S.; Cerqueira, J.R.; Ribeiro, H.J.P.S.; Garcia, K.S.; da Silva, N.N.; Queiroz, A.F. de S. Evaluation of Thermal Effects of Intrusive Rocks on the Kerogen Present in the Black Shales of Irati Formation (Permian), Paraná Basin, Brazil. *J. South Am. Earth Sci.* **2020**, *100*, 102559. [CrossRef]
51. Liu, B.; Wang, Y.; Tian, S.; Guo, Y.; Wang, L.; Yasin, Q.; Yang, J. Impact of Thermal Maturity on the Diagenesis and Porosity of Lacustrine Oil-Prone Shales: Insights from Natural Shale Samples with Thermal Maturation in the Oil Generation Window. *Int. J. Coal Geol.* **2022**, *261*, 104079. [CrossRef]
52. Delpino, D.H.; Bermúdez, A.M. Petroleum Systems Including Unconventional Reservoirs in Intrusive Igneous Rocks (Sills and Laccoliths). *Lead. Edge* **2009**, *28*, 804–811. [CrossRef]
53. Koltzer, N.; Möller, P.; Inbar, N.; Siebert, C.; Rosenthal, E.; Magri, F. Thermal Impacts of Magmatic Intrusions: A Hypothesis of Paleo-Heating Processes in the Tiberias Basin, Jordan-Dead Sea Transform. *Energy Procedia* **2017**, *125*, 80–87. [CrossRef]
54. Kim, K.; Kemeny, J.; Nickerson, M. Effect of Rapid Thermal Cooling on Mechanical Rock Properties. *Rock Mech. Rock Eng.* **2014**, *47*, 2005–2019. [CrossRef]
55. Liu, B.; Mahlstedt, N.; Horsfield, B.; Tian, S.; Huo, Q.; Wen, Z.; Pan, Z. Phase Behavior and GOR Evolution Using a Natural Maturity Series of Lacustrine Oil-Prone Shale: Implications from Compositional Modelling. *Org. Geochem.* **2023**, *185*, 104675. [CrossRef]
56. Chen, S.; Yao, S.; Wang, Y.; Liu, S.; Wang, X.; Zhang, Y.; Wang, H. Investigation of Pore Evolution and Variation with Magma Intrusion on Permian Gufeng Shale Formation and Their Implications on Gas Enrichment. *J. Nat. Gas Sci. Eng.* **2021**, *96*, 104277. [CrossRef]
57. Spacapan, J.B.; Palma, J.O.; Galland, O.; Manceda, R.; Rocha, E.; D’Odorico, A.; Leanza, H.A. Thermal Impact of Igneous Sill-Complexes on Organic-Rich Formations and Implications for Petroleum Systems: A Case Study in the Northern Neuquén Basin, Argentina. *Mar. Pet. Geol.* **2018**, *91*, 519–531. [CrossRef]
58. Bjørlykke, K.; Mo, A.; Palm, E. Modelling of Thermal Convection in Sedimentary Basins and Its Relevance to Diagenetic Reactions. *Mar. Pet. Geol.* **1988**, *5*, 338–351. [CrossRef]

Disclaimer/Publisher’s Note: The statements, opinions and data contained in all publications are solely those of the individual author(s) and contributor(s) and not of MDPI and/or the editor(s). MDPI and/or the editor(s) disclaim responsibility for any injury to people or property resulting from any ideas, methods, instructions or products referred to in the content.